Pore-scale modeling of electrical and fluid transport in Berea sandstone

Citation: Zhan, Xin, Lawrence M. Schwartz, M. Nafi Toksoz, Wave C. Smith, and F. Dale Morgan. "Pore-Scale Modeling of Electrical and Fluid Transport in Berea Sandstone." GEOPHYSICS 75, no. 5 (September 2010): F135–F142. © 2010 Society of Exploration Geophysicists

As Published: http://dx.doi.org/10.1190/1.3463704

Publisher: Society of Exploration Geophysicists

Persistent URL: http://hdl.handle.net/1721.1/85598

Version: Final published version: final published article, as it appeared in a journal, conference proceedings, or other formally published context

GEOPHYSICS, VOL. 75, NO. 5 (SEPTEMBER-OCTOBER 2010); P. F135–F142, 8 FIGS., 4 TABLES.
10.1190/1.3463704

Pore-scale modeling of electrical and fluid transport in Berea sandstone

Xin Zhan[2], Lawrence M. Schwartz[1,3], M. Nafi Toksöz[1], Wave C. Smith[3], and F. Dale Morgan[1]

ABSTRACT

The purpose of this paper is to test how well numerical calculations can predict transport properties of porous permeable rock, given its 3D digital microtomography (μCT) image. For this study, a Berea 500 sandstone sample is used, whose μCT images have been obtained with resolution of 2.8 μm. Porosity, electrical conductivity, permeability, and surface area are calculated from the μCT image and compared with laboratory-measured values. For transport properties (electrical conductivity, permeability), a finite-difference scheme is adopted. The calculated and measured properties compare quite well. Electrical transport in Berea 500 sandstone is complicated by the presence of surface conduction in the electric double layer at the grain-electrolyte boundary. A three-phase conductivity model is proposed to compute surface conduction on the rock μCT image. Effects of image resolution and computation sample size on the accuracy of numerical predictions are also investigated. Reducing resolution (i.e., increasing the voxel dimensions) decreases the calculated values of electrical conductivity and hydraulic permeability. Increasing computation sample volume gives a better match between laboratory measurements and numerical results. Large sample provides a better representation of the rock.

INTRODUCTION

Understanding the interaction between the rock matrix and pore fluids at the microscopic scale is essential for the interpretation of macroscopic geophysical measurements. With the development of modern imaging techniques, such as x-ray μCT and laser confocal microscopy, direct images (with micron resolution) of the three-dimensional (3D) pore structure of sedimentary rocks are now available. Accurate digital representations of the pore structure allow us to compute rock properties from basic physical laws (Hazlett, 1995; Coles et al., 1996; Pal and Stig, 2002). Computational rock physics has become a significant complement to core-derived laboratory measurements and empirical relationships in the interpretation of borehole measurements.

In this study, we use finite difference (FD) techniques to solve the Laplace equation for electrical conductivity and the Stokes equation for single-phase fluid flow (Schwartz et al., 1993; Garbozi and Douglas, 1996). A number of authors have used μCT images to calculate the electrical formation factors of by treating the fluid-filled porous rock as a two-phase system (Auzerais et al., 1996; Arns et al., 2001; Pal and Stig, 2002; Arns et al., 2005). The solid matrix is nonconductive and the pore fluid has a uniform conductivity. In this case, Archie's law (Archie, 1942) describes the linear relationship between fluid conductivity σ_f and saturated rock conductivity σ_{eff}. The ratio of $\sigma_f/\sigma_{\text{eff}}$ is defined as formation factor F, which is expressed as Φ^{-m}. Porosity is denoted by Φ, and m is the cementation exponent, which depends on lithology. This relationship is based on the assumption that the mobile ions are distributed uniformly throughout the pore space. Once the basic quantities of electrical and fluid flow are in hand, we go on to consider two issues related to the pore grain interface (i.e., the grain surface). While F depends on the porosity only, fluid permeability k depends also on the absolute dimensions of the pore space. Two of the simplest length scales are the ratio of pore volume to surface area V_t/S and the Λ parameter, a dynamic length derived from the solution of the conductivity problem (Brace, 1977; Johnson et al., 1986). We show that both V_t/S and Λ can be used to estimate k.

In addition to bulk conduction, there is also the mechanism of interface conduction. The surface of both quartz and clay grains becomes charged when in contact with an electrolyte. Surface conductivity is confined to a thin layer known as the electric double layer (EDL) (Debye and Hückel, 1923; Morgan et al., 1989). One of the most popular empirical models to treat surface conductivity is the Waxman-Smits model (Waxman and Smits, 1968). The model assumes that interfacial and bulk conduction simply can be added in parallel. The Waxman-Smits model is expressed as $\sigma_{\text{eff}} = (\sigma_f$

Manuscript received by the Editor 23 July 2009; revised manuscript received 13 November 2009; published online 5 October 2010.
[1]MIT, Earth Resources Laboratory, Cambridge, Massachusetts, U.S.A. E-mail: schwartz2@slb.com; toksoz@mit.edu; morgan@erl.mit.edu.
[2]Formerly MIT, Earth Resources Laboratory, Cambridge, Massachusetts, U.S.A. E-mail: xinzhan@mit.edu. Currently Exxon Mobil Upstream Research Company, Houston, Texas, U.S.A. E-mail: xin.zhan@exxonmobil.com.
[3]Schlumberger-Doll Research, Cambridge, Massachusetts, U.S.A. E-mail: schwartz2@slb.com; wsmith@boston.oilfield.slb.com

$+ BQ_v)/F^*$, where F^* is the formation factor in the low-resistivity limit, Q_v is the cation concentration per unit pore volume (meq ml^{-1}) and B is the average mobility of the counterions close to the grain surface (mho cm^2 meq^{-1}). The value of B can be adjusted to capture the nonlinear (convex-upward) behavior of σ_{eff} versus σ_f for shaly sands.

Recent authors have devoted considerable attention to treating surface conduction at the pore scale (Devarajan et al., 2006; Jin et al., 2009; Motealleh et al., 2007). In these papers, shaly sands are modeled with surface-conductive clay coating the grains. To represent shale, they assume the grains to be comprised entirely of conductive clays. However, all these calculations are based on synthetic porous media, sphere packs with a single type of clay mineral. Real rocks are known to have much more complex composition, mineral distribution, and pore geometry. Thus, one of the main objectives of this work is to numerically model surface conductivity on real rock microstructure. In addition, laboratory data are collected to verify our numerical calculations.

SAMPLE DESCRIPTION AND LABORATORY MEASUREMENTS

Our sample is a Berea Sandstone 500 (BS500) core with 23.6% porosity. A 3D μCT image was obtained from the Australia National University (ANU) Digital Core Laboratory Consortium. The gray-scale image, with brightness corresponding to X-ray attenuation, was segmented to separate the pore space and the rock matrix. This gives an 1840^3 image with a voxel size of 2.8 μm. Five 400^3 subvolumes at different locations were selected within the 1840^3 volume (as shown in Figure 1a) to capture both vertical and horizontal heterogenerity

Berea Sandstone 500 contains some clay; its mineralogy is summarized in Table 1. The presence of low-density pore inclusions (e.g., microporosity, clay, feldspars decaying into grains, etc.) leads to a spread in the intermediate portion of the attenuation histogram between the two main peaks (Pike, 1981; Minnis, 1984; Knackstedt et al., 2004; Arns et al., 2005). Figure 1a shows an example; the solid phase is divided into quartz (white) and nonquartz minerals (gray). Our ability to determine the spatial relationship of different minerals and the size of clay particles is limited by image resolution. Accordingly, we have chosen to work with the segmented image, which represents well the porosity of the interconnected pore volume and contains negligible intragranular porosity (Nelson, 2000; Wu, 2004).

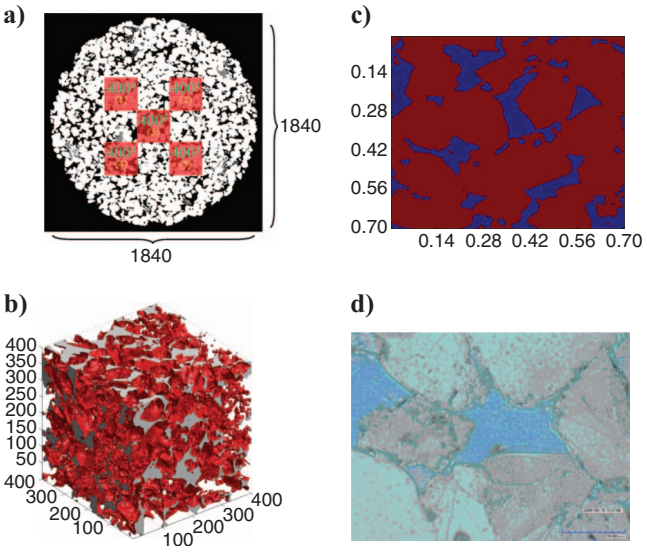

Figure 1. (a) View of selected five 400^3 subvolumes at different locations in the total 1840^3 BS500 core sample with a resolution of 2.8 μm. This is a segmented image with pore in black, quartz in white, and nonquartz components in gray. (b) Pore-cast for subvolume 3 from the middle of the total volume. (c) 200^2 subset from subvolume 3 showing absolute units. (d) Thin section for Berea 500 showing quartz grains and additional mineral inclusions.

This is a reasonable and reliable starting point for determining transport properties.

Laboratory measurements were made on a cylindrical BS500 core sample of length 3.7 cm and diameter 2.5 cm; results are summarized in Table 2. The formation factor was obtained using a NaCl brine with conductivity 0.2 S/m at 25°C. Two permeability measurements were carried out. Gas permeability was measured using nitrogen (N_2); the result of 858 mD can be converted to a liquid permeability of 430 mD, using the Klinkenberg correction (Klinkenberg, 1941; Tanikawa and Shimamoto, 2006). Direct liquid permeability was measured to be 450 mD using steady-state flow in the pressure range of 0.05 to 0.2 atm. The Brunauer-Emmett-Teller (BET) surface area was measured by adsorbing Krypton gas at successive pressures (the relative pressure P/P_0 is between 0.06 and 0.19).

A special-purpose laboratory procedure was designed to measure the electrical conductivity as a function of brine salinity. A particular concern when saturating with highly resistive electrolytes is chemical changes in the sample, such as clay swelling and liberation (Waxman and Smits, 1968; Sen and Kan. 1987). To avoid this problem, we used one freshly cut sample for each salinity. Samples were cut into cylinders of length 2 cm and diameter 2.5 cm from the original BS500 block. Ten samples were saturated with NaCl brines with conductivities ranging between 0.001 S/m and 2 S/m. Saturated samples were held by a rubber jacket to prevent them from falling apart and never allowed to dry out during the conductivity measurements, in a manner similar to the permeability measurement. Nonpolarized Ag/AgCl electrode disks were used for the conductivity measurements.

NUMERICAL CALCULATIONS

Basic electrical and fluid transport

In a composite material, the local value of the conductivity $\sigma(r)$ depends on spatial coordinate r. For steady-state conduction, the charge conservation requirement is embodied in the Laplace equation:

Table 1. Mineralogy of Berea Sandstone 500 core sample obtained by Fourier transform infrared spectroscopy.

Composition	Weight fraction(%)
Quartz	88.9
Clay	3.9
Feldspar	3.4
Carbonate	2.2
Evaporite	0.5
Others	1.1

$$\nabla \cdot \vec{J}(r) = -\nabla \cdot (\sigma(r) \cdot \nabla \vec{V}(r)) = 0. \quad (1)$$

Here, J is the current density, and V is the electrostatic potential. Because $\sigma(r) = 0$ in the insulating grains, the boundary conditions require that the current density normal to the interface must vanish while the potential is continuous. We calculate the macroscopic conductivity of the random material by applying a uniform electric potential gradient across the sample. Then the volume-averaged current density is used to compute the effective conductivity from Ohms' law.

For numerical calculation, we use a staggered-grid FD scheme with second-order accuracy in space (Moon and Spencer, 1953; Garbozi and Douglas, 1996; Zwillinger, 1997). The grid interval in the x-, y-, and z-directions is exactly the same as the μCT image resolution, 2.8 μm. Our FD electrical conductivity programs can handle isotropic materials and conductivity tensors. To calculate the formation factor, we assign $\sigma = 0$ for the solid and $\sigma_f = 1$ for the pore fluid; the fluid-filled rock conductivity σ_{eff} then equals $1/F$. The laminar flow of an incompressible fluid through a solid matrix is governed by the linear Stokes equations for the local pressure and velocity fields. We have used an industry standard FD code developed at the National Institute of Standards and Technology (ftp://ftp.nist.gov/pub/bfrl/bentz/permsolver/). This Stokes solver has been applied to a variety of 3D microstructures (Schwartz et al., 1993; Martys and Garboczi, 1992; Bentz and Martys, 2007). In the present case, a pressure gradient is applied to the μCT image, the pressure being constant on each of the opposing image faces. The local pressure is defined in the center of each voxel and the local velocity is defined at the center of each voxel edge. At the pore-grain interface, we require that the fluid velocity vanish and the pressure be continuous. The permeability κ of the porous medium is calculated by volume averaging the local fluid velocity and applying the Darcy equation

$$u = -\frac{\kappa}{\eta}\frac{\Delta P}{L}. \quad (2)$$

Here u is the average fluid velocity in the direction of the flow, ΔP is the applied pressure difference, L is the length of the sample, and η is the fluid viscosity.

Surface area

To quantify the surface area from the segmented (i.e., binary) μCT binary image, we need to identify pixels at the pore-grain interface. Unlike previous authors, who have used statistical functions, e.g., two-point correlation functions (Blair et al., 1996; Torquato and Stillinger, 2002), we use two different image-processing methods in this work. The first method is gradient-based edge detection (Canny, 1986; Pathegama and Gol, 2004), in which an odd symmetric filter (Marr and Hildreth, 1980)

$$\begin{bmatrix} -1 & 0 & -1 \\ -1 & 0 & -1 \\ -1 & 0 & -1 \end{bmatrix}$$

approximates a first derivative. Peaks in the convolution output determine the location of the pore-grain interface. The second method is based on tracing phase connectivity to identify a phase change. Voxels in the binary image are classified into two groups, inner cells and surface cells. Picturing each voxel at the center of a nine-cell unit (i.e., 3×3 cells), we check the connectivity of each phase by testing the eight neighbors of the center cell. Zero-connectivity voxels are isolated cells and are eliminated; then the surface cells are identified easily (Zahn, 1971; Zhang and Wang, 2005). The difference between results from the two methods is within 8% and we take their average as our count of the surface pixels. An example of our surface-area calculations is shown in Figure 2. Surface area is usually expressed as square meters of surface per gram of solid. Taking 2.65 g/cm^3 as the grain density, we obtain the results given in Table 3. Our numeri-

Table 2. Comparison of laboratory measurements with calculated values. The numerical values are the mean value (bold italicized number in column 3) and variance for the five subvolumes.

	Laboratory	Numerical
Porosity (%)	23.56	***23.64*** ± 0.43
Formation factor	13.03	***16.40*** ± 3.76
Permeability (Darcy)	0.45	***0.60*** ± 0.23
Surface area (m^2/g)	0.93	***0.77*** ± 0.02

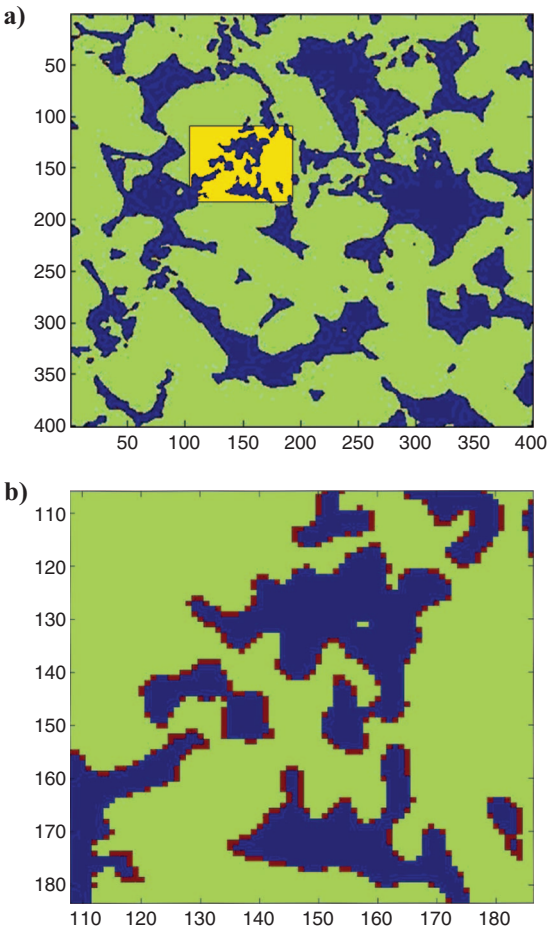

Figure 2. (a) Surface pixels (red) along the pore-grain (blue-green) boundary derived from gradient-based image processing. This is one slice in subvolume 3. (b) Enlarged view of shadowed area (yellow square) in Figure 3a.

cal calculations and the low-pressure BET measurements both provide the surface area of the sandstone skeleton.

CALCULATION RESULTS AND COMPARISON TO LABORATORY MEASUREMENTS

Five 400^3 subvolumes at different locations were selected in the total 1840^3 volume as shown in Figure 1. Subvolume 3 is in the middle of the sample. Subvolumes 1, 2, 4, and 5 are located, respectively, northwest, northeast, southwest, and southeast of subvolume 3 to capture both vertical and horizontal heterogeneity. The hydraulic flux and the electrical current density for one slice in subvolume 3 are color mapped (on a logarithmic scale) in Figure 3. For display purposes, we chose a 200^3 subvolume in the middle of subvolume 3 (Figure 3a); the most complex pore geometry was found to be in the x-y plane (Figure 3b). As expected, the electrical current shows higher amplitude than the hydraulic flux in the thin and narrow pores (Figure 3c and d). It is interesting to compare our calculations to those of Jin et al. (2009), who use random-walk methods to describe electrical conduction in 3D sphere-pack models (Finney, 1970). These methods are quite efficient and give accurate values for the conductivity but they do not yield the electric fields in the pore space as shown in Figure 3. We will see that the local electric fields also are useful in correlating electrical and fluid flow and in the description of excess surface conduction.

Porosity, formation factor, permeability, and surface area of the five subvolumes computed from the 3D μCT are listed in Table 3. The total variation in porosity is about 3%, which indicates that our calculation size is representative. Heterogeneity of the geometry at different locations of the core sample is reflected in both formation factor and permeability. An isolated inclusion, small in volume, could block the flow without much impact on porosity (Kameda, 2004). We calculate the mean value and variance for those five sets of data and compare these with the laboratory measurements in Table 2. Calculated mean values compare well with the laboratory measurements.

Formation factor and permeability correlation

Correlating hydraulic permeability to other physical properties of the porous media is an important topic. The most popular correlation relates permeability with electrical conductivity, based on the assumption that electrical and fluid streamlines are identical. On physical grounds, we have to introduce a length scale because permeability has dimensions of area. Typically, the proposed correlations have the form

$$\kappa_{\text{est}} = CR^2/F, \tag{3}$$

where C is a dimensionless constant and R is a length related to the size of the connected pore pathways (Paterson, 1983). In the simplest approach, we can use $R = V_t/S$, the pore volume to surface ratio. In a related but generally better approximation, V_t/S is replaced by the Λ parameter (Johnson et al., 1986), in which the value of the local square magnitude of the electric field is used to weight the average over the pore volume and the pore-grain interface. Because we have a complete solution of the Laplace equation, we can calculate Λ its value for each subvolume is given in Table 3. In Figure 4, these two estimates for permeability are compared to the results of our FD calculations. The agreement is good except for subvolume 4. In this subvolume, we see that the formation factor is quite low, although κ_{calc} is only slightly high and both V_t/S and Λ are large. This indicates a system with a large number of narrow channels that promote electrical transport but have relatively little influence on fluid flow. Another way to see this is to notice that in Table 3, the subvolumes with the largest (smallest) F values have the smallest (largest) surface area.

Surface-conductivity calculation and laboratory measurements

Our aim is to calculate surface conduction based on realistic pore and grain shapes defined by the BS500 μCT image. By contrast, in previous studies the solid grains were modeled as spheres (Johnson et al., 1986; Lima and Sharma, 1990; Devarajan et al., 2006; Motealleh et al., 2007; Toumelin and Torres-Verdin, 2008). Given the sparse distribution of nonquartz minerals in BS500 (gray in Figure 1a), the dominant mechanism for surface conduction is the electric double layer (EDL) lying along the entire grain-electrolyte interface.

As before, our calculations are carried out on cells with an edge length of 2.8 μm. The pore fluid is divided into free water and bound water, which exists along all the grain-electrolyte boundary. Thus surface voxels form a third phase in our conductivity calculations, as illustrated in Figure 5a. In this model, the first kind of cell has $\sigma_1 = 0$ for the insulating rock matrix, the second kind of cell has conductivity σ_2 corresponding to the bulk electrolyte, and the third kind

Table 3. Numerically computed porosity, permeability, formation factor, and surface area, ratio of pore volume to surface area, and Λ parameter for the five selected subvolumes in Figure 1a.

	1	2	3	4	5
Porosity (%)	22.98	23.33	23.81	24.10	23.60
Formation factor	22.23	18.69	16.11	11.98	16.31
Permeability (Darcy)	0.38	0.61	0.75	1.05	0.83
Surface area (m^2/g)	0.88	0.81	0.78	0.69	0.77
Ratio of pore volume to surface (μm)	6.57	7.19	7.46	8.4	7.52
Λ (μm)	6.48	7.51	8.24	10.18	8.18

of cell, containing the EDL and located at the fluid-solid interface, has conductivity σ_3. Based on the thin EDL assumption, the two conduction paths in the interface cells can be treated, to first order, as conductors in parallel (Figure 5b). The surface conductance Σ_{surf} in the EDL and the bulk conductance Σ_{bulk} in the rest of the cell can be summed to give the conductance of the surface voxel. And σ_3 is expressed as

$$\sigma_3 = \frac{\Sigma_{surf} + \Sigma_{bulk}}{L} = \frac{\Sigma_{surf} + \sigma_2.(L - \chi_d)}{L}. \quad (4)$$

Here, χ_d is the thickness of the EDL, L is the length of the cell edge and Σ_{surf} is surface conductance (with units of S) over the pore-grain interface (Schwartz et al., 1989).

To quantify surface conductance, we adopt a practical method that directly uses the CEC value of the rock sample (Kan and Sen, 1987; Sen et al., 1990; Revil and Glover, 1997, 1998; Revil et al., 1998; Revil and Leroy, 2001):

$$\Sigma_{surf} = \frac{2}{3}\left[\frac{\phi}{1-\phi}\right]\beta_s Q_v \Lambda, \quad Q_v = \rho_m[(1-\phi)\phi]CEC. \quad (5)$$

Here, ρ_m is grain density, ϕ is the porosity and β_S is the surface mobility of the counterions, which is independent of electrolyte conductivity (at least above 10^{-3} mol L^{-1}) and clay mineralogy (Shubin et al., 1996; Revil et al., 1998; Mojid and Cho, 2008). The CEC indicates the maximum number of exchange counterions per unit mass of the rock. The cation concentration per unit pore volume is denoted as Q_V, which appears in equation 2. In this way, we transfer the Q_V value (in per-unit pore volume) to Σ_{surf} (in per-unit pore surface area) through Λ, which is a weighted surface-to-volume ratio (O'Konski, 1970; Kan and Sen, 1987; Schwartz et al., 1989). This is compatible with our assumption that every surface voxel has the same effective conductivity. The Λ parameter also gives the proper geometrical factors that map conduction in the EDL and the bulk effectively into two conductors in parallel (Kan and Sen, 1987). For sodium chloride electrolyte, the counterions in the electrolyte are Na^+ with a surface mobility $\beta_s = 5.14 \times 10^{-9}$ $m^2\,s^{-1}\,V^{-1}$ at 25°C (Patchett, 1975). We substitute the measured CEC value [0.27 meg/100 g] and the computed Λ value (listed in Table 3) into equation 7 to calculate the surface conductance Σ_{surf}.

The last parameter to be determined is the EDL thickness (the Debye length) (Morgan et al., 1989; Pride and Morgan, 1991; Zhan et al., 2009):

$$\chi_d = \sqrt{\varepsilon_f \kappa_B T / e^2 z^2 N}. \quad (6)$$

Here ε_f is the fluid permittivity, κ_B is the Boltzman constant, T is the absolute temperature, e is the electric charge, z is the ionic valence of the solution, and N is the ion concentration defined as $N = 6.022 \times 10^{26} \times$ molarity. Debye lengths for different values of the brine conductivity were computed from equation 8 and are listed in Table 4. Also given in Table 4 are the corresponding values of the surface conductivity σ_3. These results comprise the input data for our three-phase solutions of the Laplace equation within the μCT structure; we can calculate σ_{eff} for a wide range of salinities.

Laboratory measurements (triangles) and numerical calculations (dashed and solid red lines) are shown in Figure 6. In the high salinity region, the two-phase model works well to predict the linear relationship between the saturated-rock conductivity σ_{eff} and the electrolyte conductivity σ_f. In this regime, the ratio σ_f/σ_{eff} is the formation factor. When the electrolyte conductivity is low and surface conductivity cannot be neglected, the three-phase model is needed to match the experimental data and the concave upward shape of the σ_{eff} versus σ_2 curve. Also shown in Figure 6 is a curve based on the Waxman-Smits equation (solid green line). Here we have taken their parameters for B in equation 2: $B = 0.046\ [1 - 0.6\ \exp(-\sigma_f/(0.013))]$, where σ_f is expressed in mho cm^{-1}. This choice leads to an over estimate of rock conductivity at low salinities. The form of B was chosen by Waxman and Smits to fit conductivity data at mostly medium to high salinities (above 0.2 S/m). The decrease of B with salinity described by their model is controversial (Schwartz, 1989; Revil et al., 1998).

In addition to the practical models using Qv as the key parameter, we also have examined the most basic electrochemical model adopted by Morgan (Morgan et al., 1989). Surface conductance Σ_{surf} is obtained by the multiplication of σ_f, and EDL thickness χd with a hyperbolic function of the normalized zeta potential (Overbeek, 1952; Morgan et al., 1989). With an estimated zeta potential as a function of σ_f, (Pride and Morgan, 1991), we obtain a value of Σ_{surf} close to that given by equation 5. The basic mechanisms of surface conduc-

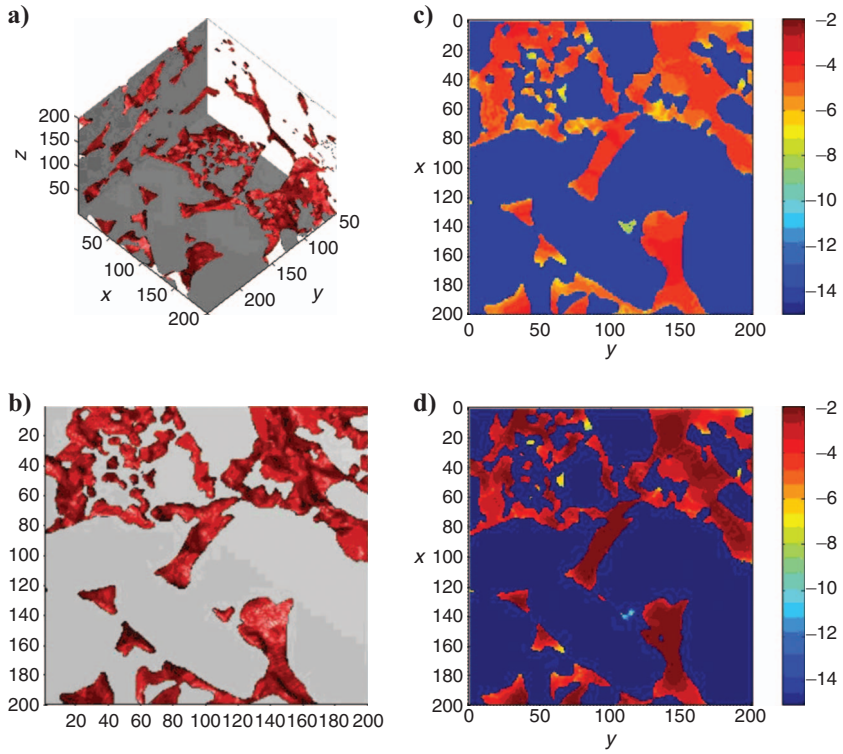

Figure 3. (a) Three-dimensional tilted view of a 200^3 cube taken from subvolume 3 (red indicates pore space, gray indicates grain). (b) The x-y plane of the first slice from Figure 3a. (c) Electrical current density for Figure 3b (on a logarithmic scale). (d) Hydraulic flux for Figure 3b (on a logarithmic scale).

tion, especially in the low-salinity regime, remain the subject of active research. Our approach is based on: (1) the measured CEC value, (2) the Λ parameter obtained by resolving the electric field in the microstructure, (3) a constant value for the surface mobility β_S, and (4) an interface conduction path along the entire grain-electrolyte boundary.

EFFECTS OF IMAGE RESOLUTION AND COMPUTATION SIZE

Image resolution

The fact that we are using finite-size voxels limits our ability to resolve the smallest features of the pore space. To test the importance of this effect, we have generated a sequence of models with successively poorer resolution by doubling the voxel edge length. Eight high-resolution voxels form one low-resolution voxel with a simple majority rule used to assign the new voxel to be either pore or grain. If more than four of the original voxels were in the pore (grain) space, the new voxel is assigned to be pore (grain); if the breakdown of the original voxels is four grain and four pore, then the new voxel is assigned randomly. Note that this is slightly different than the procedure used by Jin et al. (2009); they assign the four-four case to the grain space, which leads to decreasing porosity as the resolution is degraded. The five models then vary from the original 400^3 with resolution of 2.8 μm to 25^3 with resolution of 44.8 μm. Four downscaled cubes from the original 400^3 cube (subset 3 in Figure 1a) are shown in Figure 7. The connectivity of pore space is largely reduced with decreasing resolution. The structure of the medium is severely compromised in the model with cell size 44.8 μm.

Porosity, permeability, formation factor, and surface area were calculated for the five models; their fractional change relative to the original 400^3 with resolution of 2.8 μm is plotted in Figure 8. We note that the purely geometric parameters (porosity and surface area) are relatively unaffected and the electrical conductivity is most af-

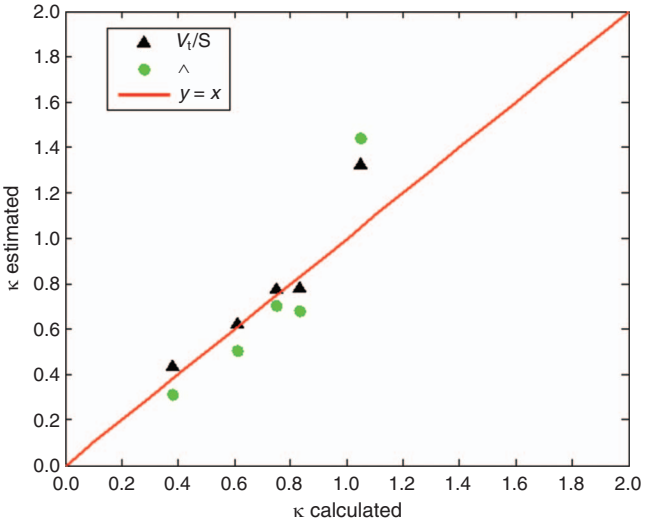

Figure 4. Numerically calculated permeability versus estimated permeability. In the estimate based on V_t/S, the value of $C = 0.225$ in the Λ estimate, $C = 0.167$.

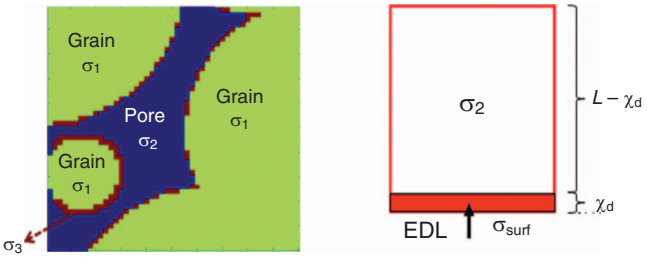

Figure 5. (a) The three-phase representation of a porous rock: σ_1 is the conductivity of solid grain, σ_2 is the free electrolyte conductivity, and σ_3 is the conductivity assigned to interface cells containing both free electrolyte and bound water. (b) Our model for the interface cells. The cell edge is L, and the EDL thickness is χ_d. Within the EDL, the conductivity is σ_{surf}. The remainder of the cell has conductivity of σ_2.

Table 4. Debye length $\mathcal{X}_d$, free-electrolyte conductivity σ_2, and surface-cell conductivity σ_3 values used in the three-phase conductivity model.

Brine conductivity σ_2 (S/m)	Debye length $\mathcal{X}_d$ (Å)	Surface-cell conductivity σ_3 (S/m)
0.005	240	0.012
0.01	166	0.015
0.025	105	0.030
0.05	74	0.055
0.1	52	0.114
0.2	37	0.205
0.4	26	0.4
1	16	1
2	12	2
10	5.3	10
50	2.4	50

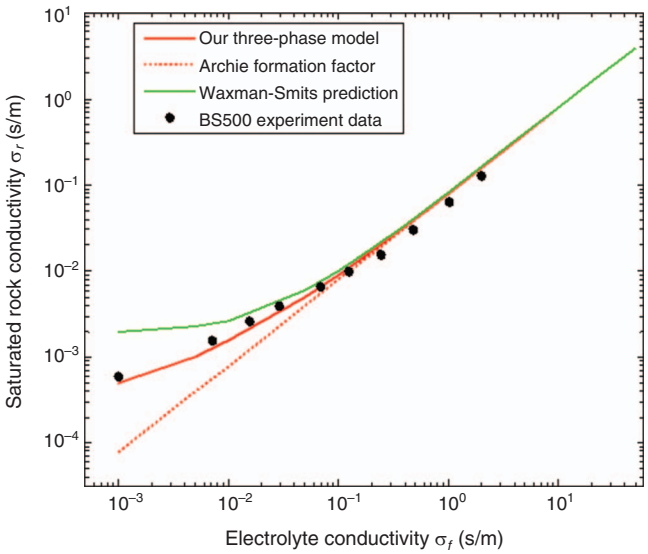

Figure 6. Three-phase conductivity calculations of the effective BS500 conductivity (solid red line) are compared to the Waxman-Smits prediction (solid green line) and experimental data for ten brine salinities (black circles). Red dashed line is the linear relationship (with Archie's formation factor) between electrolyte conductivity and saturated rock conductivity.

fected. This is expected because using coarser cells to resolve a structure tends to describe the curved grain boundaries inaccurately and to close narrow pores. Although closing a few narrow channels will not affect surface area greatly, the impact on transport properties is dramatic. As discussed in connection with Figure 3c and d, electrical current is more severely affected than hydraulic current. When the image resolution is degraded to the point where the voxel edge is larger than typical channel diameters (Table 3), the estimation of transport properties is quite poor. Thus, a marked decrease in permeability and electrical conductivity is observed when the cell size goes from 5.6 to 11.2 μm. By contrast, when we go from 2.8 to 5.6 μm, there is relatively little change in the transport properties because the pore throats are fairly well resolved. We note that our results do not exhibit the simple linear trend described in Figure 1c of Arns et al. (2001) in their analysis of calculations based on Fontainebleau sandstone microtomograms.

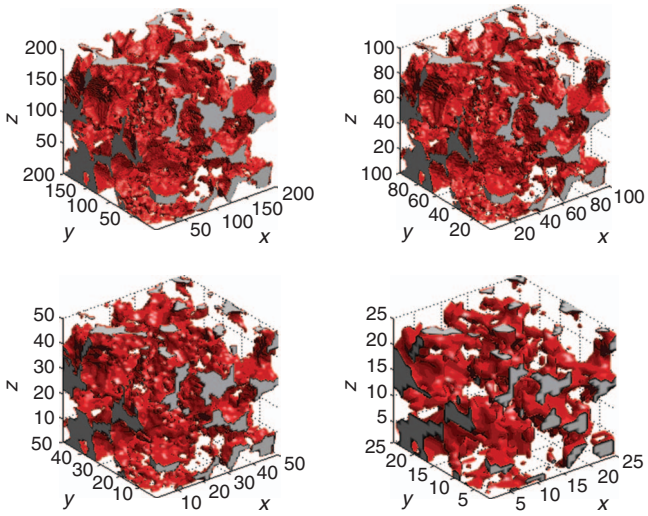

Figure 7. Three-dimensional pore structure of downscaled cubes from the original 400^3 cube (Figure 1b) using the majority rule. Connectivity of the pore space and narrow pore throats is decreasing as the image resolution degrades.

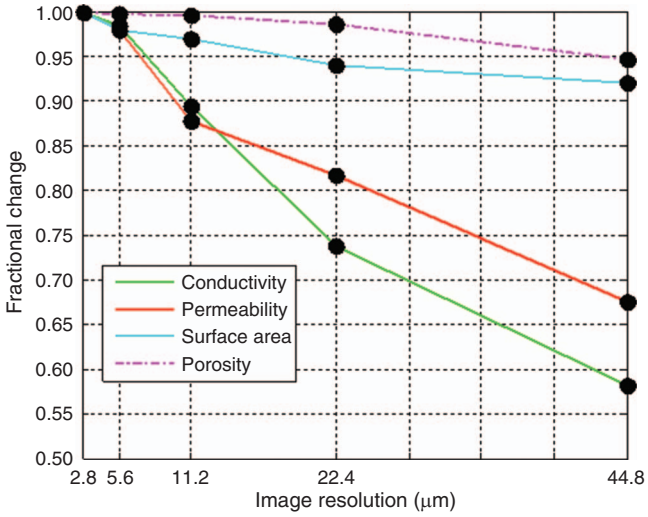

Figure 8. Fractional change in numerically computed porosity, electrical conductivity, permeability, and surface area from a 400^3 cube with a resolution of 2.8 μm to a 25^3 cube with a resolution of 44.8 μm.

Effects of computation size

We consider the effect of enlarging our model from 400^3 to 800^3, both with 2.8-μm resolution. We optimized the Laplace solver to allow dynamic allocation of memory. A single conductivity run at 800^3 cube scale requires ~10 Gbytes of memory and 15 CPU hours to complete on an Intel quad-core Xeon 3-GHz processor. In the 800^3 model, we get 13.75 for the electrical formation factor, which is much closer to the experimental value than taking the average of five 400^3 subvolumes. Thus, the choice of representative computation cell size is important. Within the capacity of computational power, a large sampling volume is preferable here.

CONCLUSIONS

In this paper, electrical and fluid transport properties of a Berea Sandstone with 23.6% porosity are computed from an X-ray μCT image and compared with laboratory measurements. Finite difference techniques are used to solve Laplace's equation for electrical conductivity and Stokes' equation for viscous fluid flow. Two different image-processing methods are applied to identify surface voxels in the digital binary image.

For computation, we chose five 400^3 subvolumes at different locations within the core. Each corresponds to a physical sample of 1 mm^3. The computed physical properties varied between subvolumes: formation factor by a factor of two (12 to 22), permeability by a factor of three (0.38 darcy to 1.05 darcy), and surface area from 0.69 m^2/g to 0.88 m^2/g. These variations are due to the heterogeneity of the BS500 at the mm scale.

The average values of properties calculated for five samples compared well with laboratory-measured values. To obtain representative values of physical properties, it is necessary to do calculations on several subsamples. Optimization of our computation algorithm enabled us to perform calculations on a large (800^3) 3D volume; this calculation gives better results for the electrical formation factor.

The effects of image resolution on computed physical properties were investigated. Decreased resolution leads to sharply decreased permeability and electrical conductivity. Good results were obtained to support a correlation linking permeability to electrical conductivity through the calculated geometric and dynamic length scales.

A three-phase conductivity model was developed to treat surface conduction based on the rock μCT image. This model agrees with experimental data and provides a better fit than the Waxman-Smits equation.

ACKNOWLEDGMENTS

This work was supported by Schlumberger-Doll Research and the MIT Earth Resources Laboratory Founding Member Consortium.

REFERENCES

Archie, G. E., 1942, The electrical resistivity log as an aid in determining some reservoir characteristics: AIME Transactions, **146**, 54–62.
Arns, C. H., F. Bauget, A. Ghous, A. Sakellariou, T. J. Senden, A. P. Sheppard, R. M. Sok, W. V. Pinczewski, J. C. Kelly, and M. A. Knackstedt,

2005, Digital core laboratory: Petrophysical analysis from 3D imaging of reservoir core fragments: Petrophysics, **46**, 260–277.
Arns, C. H., M. A. Knackstedt, and W. V. Pinczewski, 2001, Accurate estimation of transport properties from microtomographic images: Geophysical Research Letters, **28**, 3361–3364.
Auzerais, F. M., J. Dunsmuir, B. B. Ferréol, N. S. Martys, J. Olson, T. S. Ramakrishnan, D. H. Rothman, and L. M. Schwartz, 1996, Transport in sandstones: A study based on three dimensional microtomography: Geophysical Research Letters, **23**, 705–708.
Bentz, D. P., and N. S. Martys, 2007, A stokes permeability solver for three-dimensional porous media: National Institute of Standards and Technology, Internal Report 7416.
Blair, S. C., P. A. Berge, and J. G. Berryman, 1996, Using two-point correlation functions to characterize microgeometry and estimate permeability of synthetic and natural sandstones: Journal of Geophysical Research, **101**, 20359–20375.
Brace, W. F., 1977, Permeability from resistivity and pore shape: Journal of Geophysical Research, **82**, 3343–3349.
Canny, J., 1986, A computational approach to edge detection: IEEE Transactions on Pattern Analysis and Machine Intelligence, **8**, 679–714.
Coles, M. E., R. D. Hazlett, E. L. Muegge, K. W. Jones, B. Andrews, P. Siddons, A. Peskin, and W. E. Soll, 1996, Developments in synchrotron X-Ray microtomography with applications to flow in porous media: 1996 Annual Technical Conference and Exhibition, SPE, Proceedings, SPE 36531.
Debye, P., and E. Hückel, 1923, Zur theorie der electrolyte: Physikalische Zeitschrift, **24**, 185–206.
Devarajan, S., E. Toumelin, and C. Torres-Verdín, 2006: Pore-scale analysis of the Waxman-Smits shaly sand conductivity model: Presented at the 47th Annual Logging Symposium, SPWLA.
Finney, J., 1970, Random packings and the structure of the liquid state: Proceedings of the Royal Society A, 319, 479–493.
Garbozi, E. J., and J. F. Douglas, 1996, Intrinsic conductivity of objects having arbitrary shape and conductivity: Physical Review E, **53**, 6169–6180.
Hazlett, R. D., 1995, Simulation of capillary dominated displacements in microtomographic images of reservoir rocks: Transport in Porous Media, **20**, 21–35.
Jin, G., C. Torres-Verdín, and E. Toumelin, 2009, Comparison of NMR simulations of porous media derived from analytical and voxelized representations: Journal of Magnetic Resonance, **200**, 313–320.
Johnson, D. L., J. Koplik, and L. M. Schwartz, 1986, New pore-size parameter characterization transport in pours media: Physical Review Letters, **20**, 2564–2567.
Kameda, A., 2004, Permeability evolution in sandstone: Digital rock approach: Ph.D. thesis, Stanford University.
Kan, R., and P. N. Sen, 1987, Electrolytic conduction in periodic arrays of insulators with charges: Journal of Chemical Physics, **86**, 5748–5756.
Klinkenberg, L. J., 1941, The permeability of porous media to liquids and gases: Drilling and Production Practice, **8**, 200–213.
Knackstedt, M. A., C. H. Arns, A. Limaye, A. Sakellariou, T. J. Senden, A. P. Sheppard, R. M. Sok, W. V. Pinczewski, and G. F. Bunn, 2004, Digital core laboratory: Properties of reservoir core derived from 3D images: 2004 Asia Pacific Conference on Integrated Modelling for Asset Management, SPE-87009.
Lima, O. A. L., and M. M. Sharma, 1990, A grain conductivity approach to shaly sandstones: Geophysics, **55**, 1347–1356.
Marr, D., and E. C. Hildreth, 1980, Theory of edge detection: Proceeding of the Royal Society B, **207**, 187–217.
Martys, N. S., and E. J. Garboczi, 1992, Length scales relating fluid permeability and electrical conductivity in random two-dimensional model porous media: Physics Review B, **46**, 6080–6090.
Minnis, M. M., 1984, An automatic point-counting method for mineralogical assessment: AAPG Bulletin, **68**, 744–752.
Mojid, M. A., and H. Cho, 2008, Wetting solution and electrical double layer contributions to bulk electrical conductivity of sand-clay mixture: Soil Science Society of America, **7**, 972–980.
Moon, P., and D. E. Spencer, 1953, Recent investigations of the separation of Laplace's equation: Proceedings of the American Mathematical Society, 4, 302–307.
Morgan, F. D., E. R. Williams, and T. R. Madden, 1989, Streaming potential properties of westerly granite with applications: Journal of Geophysical Research, **94**, 12449–12461.
Motealleh, S., M. Gladkikh, A. Bespalov, D. C. Herrick, and S. L. Bryant, 2007, Grain-scale modeling of electrical resistivity of 'shaly sands': 48th Annual Logging Symposium, SPWLA, 2007-SSS.
Nelson, P. H., 2000, Evolution of permeability-porosity trends in sandstones: 41st Annual Logging Symposium, SPWLA, 2000-MM.
O'Konski, C. T., 1970, Convalent polymers of water: Science, **168**, 1089–1091.
Overbeek, J. Th. G., 1952, Colloid science, v. 1: Irreversible systems: Elsevier.
Pal, E. R., and B. Stig, 2002, Process based reconstruction of sandstones and prediction of transport properties: Transport in Porous Media, **46**, 311–343.
Patchett, J. G., 1975, An investigation of shale conductivity: 16th Annual Logging Symposium, SPWLA, 1975-U.
Paterson, M. S., 1983, The equivalent channel model for permeability and resistivity in fluid saturated rock — A re-appraisal: Mechanics of Materials, **2**, 345–351.
Pathegama, M., and Ö. Göl, 2004, Edge-end pixel extraction for edge-based image segmentation: Transactions on Engineering, Computing and Technology, **2**, 213–216.
Pike, J. D., 1981, Feldspar diagenesis in Yowlumne sandstone, Kern County, California: M.S. thesis, Texas A&M University.
Pride, S. R., and F. D. Morgan, 1991, Electrokinetic dissipation induced by seismic waves: Geophysics, **56**, 914–925.
Revil, A., and P. W. J. Glover, 1997, Theory of ionic-surface electrical conduction in porous media: Physics Review B, **55**, 1757–1773.
Revil, A., and P. W. J. Glover, 1998, Nature of surface electrical conductivity in natural sands, sandstone, and clays: Geophysical Research Letters, **25**, 691–694.
Revil, A., L. M. Cathles III, S. Losh, and J. A. Nunn, 1998, Electrical conductivity in shaly sands with geophysical applications: Journal of Geophysical Research, **103**, 23925–23936.
Revil, A., and P. Leroy, 2001, Hydroelectric coupling in a clayey material: Geophysical Research Letters, **28**, 1643–1646.
Schwartz, L. M., P. N. Leroy, and D. L. Johnson, 1989, Influence of rough surface on electrolytic conduction in porous media: Physics Review B, **40**, 2450–2458.
Schwartz, L. M., N. S. Martys, D. P. Bentz, E. J. Garboczi, and S. Torquato, 1993, Cross-property relations and permeability estimation in model porous media: Physics Review E, **48**, 4584–4591.
Sen, P. N., and R. Kan, 1987, Electrolytic conduction in porous media with charges: Physics Review Letters, **58**, 778–780.
Sen, P. N., C. Straley, W. E. Kenyon, and M. S. Whittingham, 1990, Surface-to-volume ratio, charge density, nuclear magnetic relaxation, and permeability in clay-bearing sandstones: Geophysics, **55**, 61–69.
Shubin, Y. V., A. V. Zadesenets, A. B. Venediktov, and S. V. Korenev, 2006, Double complex salts $[M(NH_3)_5Cl][M'Br_4]$ (M = Rh, Ir, Co, Cr, Ru; M′ = Pt, Pd): Synthesis, X-ray diffraction characterization, and thermal properties: Russian Journal of Inorganic Chemistry, **51**, 202–209.
Tanikawa, W., and T. Shimamoto, 2006, Kinkenberg effect for gas permeability and its comparison to water permeability for porous sedimentary rocks: Hydrology and Earth System Sciences Discussions, **3**, 1315–1338.
Torquato, S., and F. H. Stillinger, 2002, Controlling the short-range order and packing densities of many-particle systems: Journal of Physical Chemistry B, **106**, 8354–8359.
Toumelin, E., and C. Torres-Verdín, 2008, Object-oriented approach for the pore-scale simulation of DC electrical conductivity of two-phase saturated porous media: Geophysics, **73**, no. 2, E67–E79.
Waxman, M. H., and L. J. M. Smits, 1968, Electrical conduction in oil-bearing sands: Society of Petroleum Engineers Journal, **8**, 107–122.
Wu, T., 2004, Permeability prediction and drainage capillary pressure simulation in sandstone reservoirs: Ph.D thesis, Texas A&M University.
Zahn, C., 1971, Graph-theoretic methods for detecting and describing Gestalt clusters: IEEE Transactions on Computers, **20**, 68–86.
Zhan, X., Z. Zhu, S. Chi, and M. N. Toksöz, 2009, Elimination of LWD (logging while drilling) tool modes using seismoelectric data: Communications in Computational Physics, **7**, 47–63.
Zhang, W. M., and S. Wang, 2005, An efficient connectivity-number-based edge detection method for binary images: Proceedings of the Fourth International Conference on Machine Learning and Cybernetics, IEEE, 18–21.
Zwillinger, D., 1997, Handbook of differential equations, 3rd ed.: Academic Press, Inc.